

The Circumbinary Disc of HD 34700A

II. Analysis of a strong dust asymmetry

D. Fasano^{1,2}, M. Benisty², J. Stadler^{1,3}, F. Zagaria², A. Ziampras^{2,8}, A. Winter⁴, J. Bae⁵, S. Facchini⁶, N. T. Kurtovic²,
E. Ragusa⁶, and R. Teague⁷

¹ Université Côte d’Azur, Observatoire de la Côte d’Azur, CNRS, Laboratoire Lagrange
e-mail: dani.ele.fasano@oca.eu

² Max-Planck-Institut für Astronomie, Königstuhl 17, 69117 Heidelberg, Germany

³ European Southern Observatory, Karl-Schwarzschild-Str. 2, 85748 Garching bei München, Germany

⁴ Astronomy Unit, School of Physics and Astronomy, Queen Mary University of London, London E1 4NS, UK

⁵ Department of Astronomy, University of Florida, Gainesville, FL 32611, USA

⁶ Dipartimento di Fisica, Università degli Studi di Milano, Via Celoria 16, Milano, Italy

⁷ Department of Earth, Atmospheric, and Planetary Sciences, Massachusetts Institute of Technology, Cambridge, MA 02139, USA

⁸ Ludwig-Maximilians-Universität München, Universitäts-Sternwarte, Scheinerstr. 1, 81679 München, Germany

Received November 21, 2025; accepted March 25, 2026

ABSTRACT

Context. ALMA observations have shown that substructures are ubiquitous in protoplanetary discs. A sub-group, the transition discs, shows large cavities and rings in dust continuum. Among these, some present very high contrast asymmetries possibly due to the presence of vortices. HD 34700A is a binary system featuring a cavity, a ring, and multiple spiral arms detected in scattered light, a prominent crescent in the ALMA continuum and a complex gas morphology possibly connected with ongoing infall.

Aims. We present new ALMA band 6 (1.3 mm) continuum images of the circumbinary disc around HD 34700A and compare them with two other systems showcasing high (≥ 30 , measured as the peak-to-azimuthal-average ratio) contrast continuum asymmetries, IRS 48 and HD 142527. We aim to characterise the crescent morphology, discuss their possible origin, and, in the case of the vortex scenario, assess the efficiency of dust trapping in these systems.

Methods. We perform visibility modelling of the new high resolution ($0''.11 \times 0''.09$) ALMA band 6 continuum data of HD 34700A, together with improved visibility modelling of the other two targets.

Results. We detect a $0''.46$ (161 au) large cavity and resolve a ring with an asymmetric crescent and an extended tail at $0''.53$ (186 au) with peak intensity of $1.9 \text{ mJy beam}^{-1}$, corresponding to the second highest contrast (~ 62) ever detected with ALMA in a protoplanetary disc. We also detect unresolved emission inside the cavity, that we attribute to an inner disc. Our visibility model is in remarkable agreement with the HD 34700A data, featuring only localised residuals in the region of the disc corresponding to the tail of the asymmetry. For HD 142527, we obtain a very good overall agreement with the data, recovering both the double peaked asymmetric ring and the inner disc emission. In the case of IRS 48 we recover the general morphology of the asymmetry, but we cannot reproduce the fainter ring. We then run a hydrodynamic model of a vortex with different dust fluids, reproducing the general morphology observed in the HD 34700A and IRS 48 systems, with the emission around the vortex showing a mild asymmetry between the leading and trailing sides.

Conclusions. With a combination of visibility, dust evolution and hydrodynamical models, we have constrained the morphology of the dust continuum emission of HD 34700A for the first time, and improved existing models for IRS 48 and HD 142527. The high azimuthal contrast of the asymmetries rules out the orbit clustering of eccentric cavities scenario, while the dust evolution models we consider suggest that the vortex scenario is a plausible option.

Key words. Planets and satellites: formation – Protoplanetary discs – Planet-disc interactions

1. Introduction

High spatial resolution observations from the Atacama Large Millimeter/submillimeter Array (ALMA) have shown a variety of substructures in the continuum emission of protoplanetary discs, such as rings, gaps and cavities (Andrews et al. 2018; Long et al. 2018; Andrews 2020; Bae et al. 2023). Systems featuring large cavities in the dust emission are typically labelled as transition discs (Strom et al. 1989; Espaillat et al. 2014). Kinematic analysis of molecular line emission shows the presence of cavities also in the gas in many transition discs (van der Marel et al. 2016b; Boehler et al. 2017; Dong et al. 2017), as well as a more complex morphology showing spiral arms and localised devia-

tions from Keplerian rotation (Wölfer et al. 2023; Izquierdo et al. 2025).

A systematic study of asymmetric transition discs was conducted by van der Marel et al. (2021). More recently, similar continuum asymmetries have been detected also in debris discs, suggesting that they might be common also in the later stages of protoplanetary discs (Marino et al. 2026; Lovell et al. 2026). These systems are of particular interest as the asymmetric emission is thought to be caused by physical processes that promote azimuthal trapping of dust grains (Birnstiel et al. 2013; Pinilla et al. 2012), and could potentially provide favourable conditions for the formation of planetesimals (Barge & Sommeria 1995; Surville et al. 2016; Surville & Mayer 2019). Az-

azimuthal dust trapping is primarily caused by the presence of a pressure maximum, with two possible mechanisms at its origin: anti-cyclonic vortices triggered by the Rossby Wave Instability (RWI), (Lovelace et al. 1999; Li et al. 2000; Lyra & Lin 2013; Baruteau & Zhu 2016) or gas horseshoes induced by eccentric cavities due to binary companions (Shi et al. 2012; Ragusa et al. 2017; Miranda et al. 2017). The Rossby Wave Instability requires a narrow dip in the vortensity radial profile, which can occur in the presence of strong density (de Val-Borro et al. 2007) or viscosity gradients (Regály et al. 2012), typically at the edge of gas rings and cavities, and can be triggered by infalling material on the disc (Bae et al. 2015). It also requires low viscosity ($\alpha \lesssim 10^{-3}$ Shakura & Sunyaev 1973; Zhu & Stone 2014) to produce long lived vortices. On the other hand gas horseshoes only need a massive binary companion (with a mass ratio of $q > 0.05$) and are not limited by the disc viscosity (Ragusa et al. 2017, 2020). Both mechanisms produce a gas azimuthal overdensity of a factor $\lesssim 2 - 4$, orbiting at Keplerian velocity, and trap millimetre dust grains both radially and azimuthally (Birnstiel et al. 2013), resulting in an azimuthal dust contrast, defined as the ratio between the peak intensity and the azimuthal average of the ring emission¹, of up to a few hundreds.

Another possible origin for continuum asymmetries is the presence of an eccentricity gradient in the disc (Ataiee et al. 2013), where the eccentric orbits of dust and gas particles cluster along the gradient direction, which is typically the apocenter for eccentric cavities in transition discs (Ragusa et al. 2024). In this scenario the overdensity remains fixed at the apocenter of the orbit, hence it does not rotate with Keplerian motion around the central star. As the overdensity is a consequence of the orbits clustering and eccentricity gradient of the disc, it also does not create azimuthal pressure variations and does not trap dust, achieving only a moderate azimuthal contrast of $\lesssim 5$ (Ataiee et al. 2013).

Differentiating between these scenarios as the cause of the observed asymmetries has been a challenging endeavour. The disc turbulence, which governs if vortices can be excited, is poorly constrained (Flaherty et al. 2020; Rosotti 2023). As a result, observations achieving an angular resolution higher than $0''.1$ and a spectral resolution of $\sim 100\text{ms}^{-1}$ (e.g. Robert et al. 2020; Huang et al. 2018) are needed to detect the characteristic gas signature associated with vortices and disentangle the origin of the dust asymmetries, although beam smearing effects can produce similar patterns (Boehler et al. 2021). van der Marel et al. (2021) studied a sample of asymmetric transition discs, but could not rule out either process. Recently, Wölfer et al. (2025) constructed an analytical vortex model and performed hydrodynamic simulations to study four discs with azimuthal dust asymmetries from the exoALMA sample (Teague et al. 2025), finding no unambiguous link between the kinematical patterns of the data and the continuum crescents, likely due to the complex underlying kinematical field.

In this paper, we present recent ALMA observations of the system HD 34700 AaAb (hereafter HD 34700 A) that resolved a prominent dust asymmetry co-located with a tentative kinematic vortex signature (Stadler et al. 2026). We focus on the continuum data of HD 34700 A and perform visibility modelling of the new ALMA Band 6 observations, comparing it with the transition discs with the most prominent asymmetries (with a con-

trast $\gtrsim 30$) from the van der Marel et al. (2021) sample, namely Oph-IRS 48 (IRS 48 hereafter) and HD 142527. This paper is organised with the following structure: in Sec. 2 we present the observations used in our analysis, while in Sec. 3 we introduce the methods adopted to model the data. In Sec. 4 we present the results of our visibility modelling and discuss them in Sec. 5; we summarise our findings in Sec. 6.

2. Observations

2.1. Sources

HD 34700 A: HD 34700 A is a near-equal-mass ($M_{\text{bin}} = 4 M_{\odot}$) close ($a_{\text{bin}} = 0.69$ au) Herbig Ae spectroscopic binary, belonging to the quadruple system HD 34700 ($d \approx 351$ pc Gaia Collaboration et al. 2023; Sterzik et al. 2005). The two young (~ 5 Myr) stars have stellar radii of $R_1 = 3.46 R_{\odot}$ and $R_2 = 3.40 R_{\odot}$ (Monnier et al. 2019), and effective temperatures of $T_{\text{eff},1} = 5900$ K and $T_{\text{eff},2} = 5800$ K (Torres 2004). Monnier et al. (2019) resolved the circumbinary disc around HD 34700 A for the first time using Gemini Planet Imager (GPI) band K and H polarized scattered light images, unveiling an elliptical ring at 175 au with an inclination $i = 42^{\circ}$ and a Position Angle (PA) of 42° , a dust depleted cavity, multiple spiral arms and a discontinuity towards the north side of the disc, later confirmed by Uyama et al. (2020) with Subaru/SCExAO and Columba et al. (2024) using SPHERE/IRDIS (H and K bands) and SPHERE/IFS (YJH bands). Additionally, Columba et al. (2024) detected a symmetric ring with inclination $i = 39.7 \pm 2^{\circ}$ and PA = $87.1 \pm 1.2^{\circ}$ in SPHERE/ZIMPOL H α scatter light observations, inside the infrared (IR) ring, at 65 – 120 au. Benac et al. (2020) imaged the 1.13 mm continuum, ^{12}CO and ^{13}CO J = 2 – 1 emission with a resolution of $0''.5$ using the Submillimeter Array (SMA), resolving a prominent dust asymmetry at 155^{+11}_{-7} au with radial width of 72^{+14}_{-15} au and azimuthal width 64^{+8}_{-7} deg, and a circumbinary disc rotating counter-clockwise.

Recent ALMA band 6 observations ($\lambda = 1.3$ mm, $0''.11$ resolution), (Stadler et al. 2026) resolved for the first time the ring co-orbital with the previously detected asymmetry, a dust depleted cavity and emission from the inner region in the continuum. We describe the dust morphology in detail in Sec. 4. Stadler et al. (2026) also performed kinematic analysis of the ^{12}CO , ^{13}CO and C^{18}O J = 2 – 1 molecular lines, tracing a $0''.20$ (≈ 65 au) inner cavity in the peak intensity maps of all the isotopologues, strong deviations from Keplerian rotation in the ^{12}CO emission in the shape of spiral spurs following the IR spiral ring, and less pronounced residuals in the ^{13}CO and C^{18}O velocity maps resembling the kinematic signature of a vortex (Wölfer et al. 2025).

IRS 48: IRS 48 is a $\sim 2.5 M_{\odot}$, ~ 4 Myr old Herbig A0 star ($T_{\text{eff}} \approx 9000$ K; Brown et al. 2012; Schworer et al. 2017; Francis & van der Marel 2020), at a distance of $d \approx 135$ pc (Gaia Collaboration et al. 2023). ALMA band 7 observations of ^{12}CO and ^{13}CO have shown a gas disc with inclination $i = 50^{\circ}$ and PA = 100° and a 20 – 30 au gas cavity (Bruderer et al. 2014; van der Marel et al. 2016a). The continuum emission features an eccentric ring ($e = 0.27$) with a semi-major axis of 78 au and the most prominent asymmetry observed at sub-mm wavelengths (with a contrast of $\gtrsim 270$) (Yang et al. 2023), interpreted as a dust trap (van der Marel et al. 2013, 2015). The asymmetry shows a tail spanning $\sim 180^{\circ}$ from the peak emission to the opposite side of the ring, that trails behind the overdensity, as the disc rotates counter-clockwise (Bruderer et al. 2014). Using

¹ For very high contrast discs, where the emission of the ring is not detected across all azimuth, a different approach is typically used, evaluating the contrast as the ratio between the peak intensity and either the emission at the same radius shifted by 180° , or the 3σ upper limit.

polarimetric ALMA data, Yang et al. (2024) attributed the asymmetric overdensity to a vortex with moderate dust settling and an effective turbulence parameter $\alpha = 10^{-4} - 5 \times 10^{-3}$.

HD 142527: HD 142527 is a binary system comprising a $\sim 1.69 M_{\odot}$ F6 star, with an age of ~ 8 Myr, stellar radius of $R \approx 2.2$ au and temperature of ~ 6500 K (Fairlamb et al. 2015; Francis & van der Marel 2020), and a $\sim 0.1 M_{\odot}$ M dwarf companion ($T_{\text{eff}} = 2600 - 2800$ K, $R \approx 0.9 R_{\odot}$; Lacour et al. 2016; Claudi et al. 2019) on an eccentric ($e \gtrsim 0.2$) and non coplanar orbit, at separations of $\sim 44 - 90$ mas (~ 15 au; Biller et al. 2012; Nowak et al. 2024) and a distance of $d \approx 157$ pc (Gaia Collaboration et al. 2023). The binary orbit is too compact to explain the large cavity, suggesting the presence of a planet shaping the disc substructures (Nowak et al. 2024). Recent MATISSE observations have shown that the circumstellar disc around HD 142527 A features a complex, asymmetric geometry, possibly associated with the interactions with the companion star (Scheuck et al. 2026). The stars are surrounded by a circumbinary disc rotating clockwise with inclination $i = 27^{\circ}$ (Fukagawa et al. 2013; van der Marel et al. 2021) and a position angle $PA = 160^{\circ}$. A double peaked asymmetry at a radial location of ~ 166 au has been observed in the ALMA band 7 continuum, with a contrast of $\gtrsim 50$ (Casassus et al. 2013; Boehler et al. 2017). The ^{12}CO and C^{18}O ALMA line emission have shown a gas cavity of 50 au, wherein a misaligned inner disc ($i = 23^{\circ}$, $PA = 14^{\circ}$ Marino et al. 2015; Bohn et al. 2022) casts shadows on the outer disc (Boehler et al. 2017). Performing kinematic analysis of these molecules, Boehler et al. (2021) found deviations of 350 ms^{-1} from the Keplerian rotation of the disc, co-located with the dust crescents, and suggesting that this could be caused by a vortex with an aspect ratio of 5, centred at the secondary peak of the dust continuum. Additionally, Temmink et al. (2023) analysed multiple molecules in this system, observing an asymmetric molecular emission in HCN and CS, peaking at the opposite side of the disc with respect to the continuum crescent. They infer that this asymmetry is likely due to continuum over-subtraction for the main CO isotopologues, and propose that it can be the result of shadowing from the misaligned inner disc for the CS and HCN molecules.

2.2. Data

In this work, we consider ALMA band 6 continuum data of the system HD 34700 A (2022.1.00760.S; PI: J. Stadler), ALMA band 7 (0.87 mm) continuum observations of the disc IRS 48 (2019.1.01059.S; PI: H. Yang) and ALMA band 7 continuum data of the system HD 142527 (2013.1.00305.S; PI: S. Casassus).

The HD 34700 data consists of two short baseline (SB) and 11 long baseline (LB) execution blocks (EBs). The SB data were taken on October 9, 2022, in configuration C-3 (maximum baseline $L_{\text{max}} = 500$ m) and with a mean Precipitable Water Vapour (PWV) of 0.3 mm. The LB data were taken in configuration C-6 ($L_{\text{max}} = 2.5$ km) over a period of three weeks, on May 13, 19, 21, 24, 28, 30, and June 2, 2023, using a number of antennas between 42 and 44 and with a mean PWV in the range 0.3–1.4 mm. The spectral setup was chosen to study the kinematics of the system, thus only two spectral windows (SPWs) are dedicated to the continuum emission centred at 218.0 and 232.6 GHz with the maximum bandwidth of 1.9 GHz. In this paper, we focus on visibility modelling the continuum emission of HD 34700 A. However, the HD 34700 ALMA data set incorporates emission not

only from the circumbinary disc A, but also from the low-mass companion B in the same field-of-view (Stadler et al. 2026). We first start by removing the contribution from the secondary from the visibility table. To do so, we create a CLEAN model of HD 34700 B CLEANing down to $5 \mu\text{Jy}/\text{beam}$ ($\approx 1\sigma$) within an elliptic CLEAN mask of $R = 0''.625$ ($i = 41.5$) centred around B. We then remove the `tclean` model visibility from the data set using the `uvsub()` task of CASA (CASA Team et al. 2022) to obtain the final measurement set used in this work. The phase centre of the dataset is $(05^{\text{h}}19^{\text{m}}41^{\text{s}}.4115, 05^{\circ}38'42''.7931)$.

The IRS 48 observations consists of six EBs in two different array configurations, C43-6 and C43-7, and were conducted on 2021 June 7, June 14, and July 19 with a mean PWV in the range 0.6 – 0.9 mm. As the observations were aimed at measuring the dust polarization, all the SPWs were dedicated to the continuum emission, centred at 336.5, 338.4, 348.5, and 350.5 GHz, with a nominal bandwidth of 2.0 GHz. The reported phase centre is $(16^{\text{h}}27^{\text{m}}37^{\text{s}}.1700, -24^{\circ}30'35''.6710)$.

The HD 142527 data consists of two EBs in two different array configurations, C43-5 and C35-5. The observations were conducted on August 11 and 30, 2015, with a PWV of 1.6 mm and only one spw dedicated to the continuum emission, centred at 277 GHz with a nominal bandwidth of 2.0 GHz. The reported phase centre is $(15^{\text{h}}56^{\text{m}}41^{\text{s}}.8741, -42^{\circ}19'23''.6564)$.

The self-calibration strategy for the HD 34700 A, IRS 48 and HD 142527 datasets are described in Stadler et al. (2026); Yang et al. (2023); Temmink et al. (2023).

2.3. Imaging

We image the continuum data using the `tclean()` task of the CASA software (CASA Team et al. 2022), version 6.6.5-31. We define elliptic masks with semi-major axis of $1''.2$, $1''.0$, $2''.2$ and inclination of 35° , 51° , 29° for HD 34700 A, IRS 48, and HD 142527, respectively, and CLEAN the images down to 3σ using a robust parameter of 0.0, chosen to provide the best balance between resolution and sensitivity. We produce a 2000×2000 pixels image with pixel size of $0''.015$ for HD 34700 A, a 1024×1024 pixels image with pixel size of $0''.009$ for IRS 48, and a 1024×1024 pixels image with pixel size of $0''.025$ for HD 142527. We use the `gofish` package (Teague 2019) to compute the Root Mean Square (RMS) noise in annulus between $2''.5 - 4''$ for HD 34700 A and IRS 48, and between $3'' - 4''$ for HD 142527. The final images are shown in Figure 1, while their properties are summarised in Table 1.

3. Methods

We model the continuum emission of the new HD 34700 A data in order to constrain the morphological properties of the crescent and ring. van der Marel et al. (2021) already fitted the visibilities of the ALMA data for the systems IRS 48 and HD 142527, assuming a simple 2D arc to model the asymmetric rings. However, recent observations of IRS 48 also resolve a ring, while a single arc could not fully describe the double peaked emission of HD 142527, as shown by their intensity residuals of up to 40%. As a result, in this work we perform visibility fitting for the new data of HD 34700 A as well as the IRS 48 and HD 142527 data, using an improved model.

We use the code `galario` (Tazzari et al. 2018) to fit the visibility data and characterize the morphological structure of the continuum emission. We assume a 2D parametric intensity model and follow a Markov Chain Monte Carlo (MCMC) approach implemented with the package `emcee` (Foreman-Mackey

Table 1: Disc continuum properties and geometrical parameters.

System	Robust, Beam [mas×mas]	PA _{beam} [deg]	RMS noise [μJy beam ⁻¹]	Peak Intensity [mJy beam ⁻¹]	Contrast	<i>i</i> [deg]	PA [deg]	ΔRA [mas]	ΔDec [mas]
HD 34700 A	0.0, 114 × 94	87	7	1.90 ± 0.19	62	35.09 ^{+0.12} _{-0.06}	92.9 ^{+0.3} _{-0.3}	-48 ⁺¹ ₋₁	14 ⁺¹ ₋₁
IRS 48	0.5, 108 × 72	-73	16	18.0 ± 1.8	259	50.996 ^{+0.003} _{-0.005}	100.12 ^{+0.04} _{-0.04}	83.8 ^{+0.3} _{-0.3}	107.8 ^{+0.2} _{-0.2}
HD 142527	0.0, 299 × 203	79	252	85.8 ± 8.6	37	29.079 ^{+0.008} _{-0.004}	182.96 ^{+0.05} _{-0.03}	-38.1 ^{+0.2} _{-0.2}	-154.6 ^{+0.2} _{-0.2}

et al. 2013). With this procedure, we can constrain both the morphological parameters specific to the chosen model, as well as the geometrical parameters of the outer disc, namely the inclination *i*, the position angle PA and the offsets (ΔRA, ΔDec) between the disc and the phase centres.

We define three models for the brightness distribution:

$$I_{\text{HD 34700 A}}(r, \theta) = G(f_0, \sigma_0) + GR(f_1, r_1, \sigma_{r,1}) + GAA(f_1^a, r_1^a, \sigma_{r,1}^a, \theta_1^a, \sigma_{\theta,11}^a, \sigma_{\theta,r1}^a), \quad (1)$$

$$I_{\text{IRS 48}}(r, \theta) = GR(f_1, r_1, \sigma_{r,1}) + GAA(f_1^a, r_1^a, \sigma_{r,1}^a, \theta_1^a, \sigma_{\theta,11}^a, \sigma_{\theta,r1}^a), \quad (2)$$

$$I_{\text{HD 142527}}(r, \theta) = Go(f_0, x_0, y_0, \sigma_0) + GR(f_1, r_1, \sigma_{r,1}) + \sum_{i=1}^2 GAA(f_i^a, r_i^a, \sigma_{r,i}^a, \theta_i^a, \sigma_{\theta,li}^a, \sigma_{\theta,ri}^a), \quad (3)$$

where $G(f, \sigma)$ is a Gaussian aligned to the image centre with radial width σ and peak flux f , $Go(f, x, y, \sigma)$ is an offset Gaussian centred in the (x, y) coordinates, $GR(f, r, \sigma)$ is an axisymmetric Gaussian ring centred in r with radial width σ and peak flux f , while $GAA(f, r, \sigma_r, \theta, \sigma_{\theta,1}, \sigma_{\theta,r})$ is a Gaussian asymmetric arc centred in (r, θ) with radial width σ_r , azimuthal widths $\sigma_{\theta,1}$ and $\sigma_{\theta,r}$, and peak flux f . The models for HD 34700 A, IRS 48 and HD 142527 have a total of 15, 13 and 23 parameters, respectively. We use the Gaussian to describe the emission originating inside the cavity, the Gaussian ring, and the Gaussian arcs to model the asymmetric ring, choosing one arc for the single peaked emission of HD 34700 A and IRS 48, and two arcs for the double peaked morphology of HD 142527. We use asymmetric arcs with different azimuthal widths on the left ($\sigma_{\theta,1}$) and right ($\sigma_{\theta,r}$) of the peak intensity to better reproduce the tail observed in the continuum images. We choose to fix the inner Gaussian to the image centre for the HD 34700 A model due to its proximity to the ring asymmetry, as the inner Gaussian would merge with the ring otherwise. We check that fixing the Gaussian in the centre does not affect the remaining parameters of the model, as they remain within 1σ error bars when the Gaussian is not fixed in the centre. In the case of IRS 48, adding a Gaussian component to the model does not recover the emission from the inner disc. This might be caused by the extreme intensity contrast of the asymmetric emission. As a result, we choose not to use a Gaussian component in the model of IRS 48.

We perform a preliminary exploration of the parameter space with *emcee* using uniform priors, sampling f_0 , f_1 , f_1^a and f_2^a logarithmically and the remaining parameters linearly. As initial step we use 100 walkers over $\sim 10^3$ steps. We then associate the best fit parameters as the median of the posterior distribution from this preliminary exploration, and set them as initial

guesses for the fiducial *emcee* run. For each dataset we set up 120 walkers and 2×10^4 steps, and discard the first 25% steps as burn-in. We report the geometrical parameters (*i*, PA, ΔRA and ΔDec) in Table 1, while the full set of best fit parameters is shown in Table B.1, with the adopted priors reported in Appendix B. For the inclination and PA of HD 34700 A, we consider narrow priors around the values resulting from the ¹³CO discriminator (Izquierdo et al. 2021) fit in Stadler et al. (2026) to help achieve convergence, and be consistent with their analysis. We use the same procedure for IRS 48, using the inclination and PA reported in Yang et al. (2023). For HD 142527, instead, we setup wider priors around the inclination and PA reported in van der Marel et al. (2021). We then evaluate the best fit *galario* model sampling the visibility plane at the same *uv* points of the observations, obtaining synthetic visibilities for the model, and subtract them from the observed visibilities in order to obtain the residuals. We then image the best fit *galario* model and the residuals using the same procedure explained in Sec. 2.3.

4. Results

4.1. Continuum images

In Figure 1 we present the continuum image of the new ALMA band 6 data for HD 34700 A and compare it with the continuum images of IRS 48 (Yang et al. 2023) and HD 142527 (Temminck et al. 2023). In Figure 2, we show the de-projected continuum images in polar coordinates (left panel) and azimuthal profiles at {87, 112, 137, 162, 187} au, {65, 80, 95, 110, 125} au and {137, 162, 187, 212, 237} au for HD 34700 A, IRS 48, HD 142527, respectively. We perform the de-projection using the package *goFish*, assuming the geometrical parameters from Table 1, and then interpolate the resulting image on a 501×2001 (*R, θ*) grid, with $R \in [0, 4]''$ and $\theta \in [-180, 180]^\circ$.

All systems feature an asymmetric overdensity with a tail trailing with respect to the disc rotation, and emission originating inside the dust depleted cavity. In Figure 1 we also show the centre of the ring in the *galario* model. We measure the peak intensity for all the images, estimating its uncertainty as the 10% ALMA flux calibration error for band 6 and 7². We define the contrast as the ratio between the peak intensity and the azimuthal average of the ring emission³, masking the asymmetry contribution when it becomes higher than 16σ , and report their values in Table 1. This corresponds to a peak intensity of 271σ , 1125σ and 340σ and contrasts of 62, 259 and 37 for HD 34700 A, IRS 48 and HD 142527, respectively, making HD 34700 A the disc with the second most prominent contrast in continuum emission ob-

² see Sect. 10.2.6 in the ALMA Technical Handbook

³ For HD 142527 we compute the azimuthal average along the same radius of the peak intensity. For HD 34700 A and IRS 48, instead, we perform the azimuthal average along the radius at 170 au and 65 au, as the ring looks more eccentric.

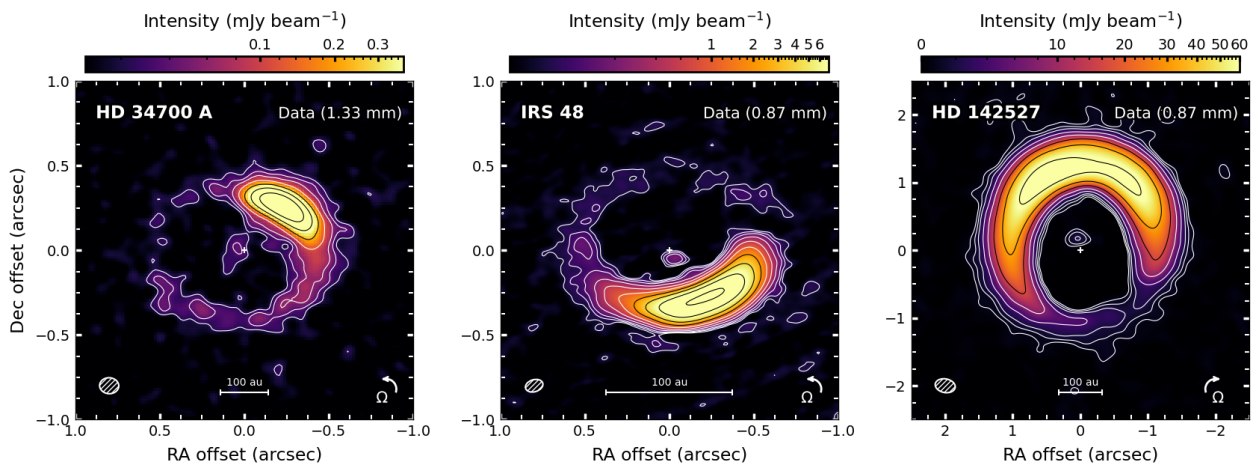


Fig. 1: Continuum images of HD 34700 A (left), IRS 48 (middle) and HD 142527 (right). The white/black contours are taken at 3σ , 5σ and $2^n\sigma$, with integer numbers $n \geq 3$. The white plus sign marks the centre of the ring in the *galarío* model, the ellipse in the bottom left corner represents the synthesised beam and the arrow in the bottom right corner shows the direction of the gas rotation. We apply an asinh stretch from $\{0.007, 0.007, 0.000\}$ mJybeam $^{-1}$ to a factor $\{0.2, 0.4, 0.7\}$ of the peak intensity, using a stretch parameter of $\{0.1, 0.01, 0.1\}$ to the colour scale to visually enhance the fainter emission.

served with ALMA to date. For reference, we also report a contrast of 45, 365 and 33 if defined as the ratio between the peak intensity and the emission at the opposite side of the disc (i.e., same radius and PA shifted by 180°).

4.2. *galarío* model and residuals

In Figure 3 we show the main results of the *galarío* modelling of HD 34700 A (top panels), IRS 48 (middle panels) and HD 142527 (bottom panels). The *galarío* model for HD 34700 A is in remarkable agreement with the data, with residuals of up to 7.4σ ($\sim 2.7\%$ of the peak intensity) localised only in the region of the asymmetric tail. The final model consists of a central Gaussian with width of $\sim 0''.13$ (46 au), a ring centred in $\sim 0''.53$ (186 au) with radial width $\sim 0''.08$ (28 au) and an arc centred at $(\sim 0''.39, 328^\circ)$ (137 au) with radial width $\sim 0''.03$ (11 au) and an azimuthal Full Width Half Maximum (FWHM) of 43.2° , which we computed as $\sqrt{2 \ln 2}(\sigma_{\theta,l}^a + \sigma_{\theta,r}^a)$. Although we fixed the inner Gaussian to the disc centre, the model still reproduces the emission remarkably well, with residuals $< 3\sigma$ in the cavity. The ring prescription we use is too simple to reproduce the faint azimuthal variations observed in the data, overestimating the intensity in the North-East side of the ring (with residuals $\leq 3\sigma$) and underestimating the tail contribution, implying that the tail structure is more complex than a simple Gaussian azimuthal dependence. Taking into account the improved resolution and S/N, our results are consistent with the SMA data presented in Benac et al. (2020), with their radial position, radial width and azimuthal FWHM of the asymmetry being within 2σ of our model fit and new data.

For IRS 48, the *galarío* model reproduces the general morphology of the asymmetry, but fails to recover the ring emission. This is probably due to the extreme contrast of the crescent, which dominates the residuals, but can also be a consequence of the eccentric nature of the ring, which is not taken into account by our model. In the region of the asymmetry we measure residuals of up to 96σ and -152σ , which correspond to deviations of 8.6% and 13.5% of the peak emission, respectively. The final model consists of a ring centred in $\sim 0''.72$ (97 au) with radial width $\sim 0''.17$ (23 au), although too faint compared with the

observations, and an arc centred at $(\sim 0''.42, 197^\circ)$ (56 au) with radial width $\sim 0''.07$ (9 au) and an FWHM of 79.0° . These values are consistent with the single arc model from van der Marel et al. (2021).

In the case of HD 142527, the *galarío* model reproduces the general morphology observed in the data at a very good qualitative level, showing both the disc and the double peaked emission in the ring. However, strong residuals of up to 20.1σ are present all across the ring, although they represent deviations of only 6.2% when compared to the peak intensity, an improvement of more than a factor 6 compared to the previous model from van der Marel et al. (2021). The final model features a Gaussian with an offset of (94, -159) mas and a width of $\sim 0''.03$, a very thin ring centred at $\sim 1''.1$ with width $0''.003$ and two asymmetric arcs centred at $(\sim 1''.2, 298^\circ)$ and $(\sim 1''.3, 227^\circ)$, with radial width of $\sim 0''.14$ and $\sim 0''.18$ and an azimuthal FWHM of 82° and 107° , in contrast with the single arc centred at 240° with an FWHM of 155° modelled by van der Marel et al. (2021). Additionally, we find an inclination and PA that differ by 2° and 23° from those reported in van der Marel et al. (2021).

5. Discussion

5.1. Dust trapping

In van der Marel et al. (2021), the authors analysed a sample of transition discs showing a variety of crescents, aiming to model them as anticyclonic vortices. They constructed emission azimuthal profiles based on the analytical model⁴ of Birnstiel et al. (2013), which computes analytically the equilibrium between azimuthal drift and mixing of dust particles, and comparing their FWHM with that extracted from the data azimuthal profiles, as a function of the observed Stokes number defined as:

$$St_{\text{obs}} = \frac{\lambda_{\text{obs}} \rho_s}{4 \Sigma_{\text{gas}}(R_{\text{dust}})}, \quad (4)$$

with λ_{obs} the observed wavelength, ρ_s the intrinsic dust density and $\Sigma_{\text{g}}(R_{\text{dust}})$ the gas density at the ring location (R_{dust}). Then, they model the gas surface density distribution as

⁴ https://github.com/birnstiel/azimuthal_profile

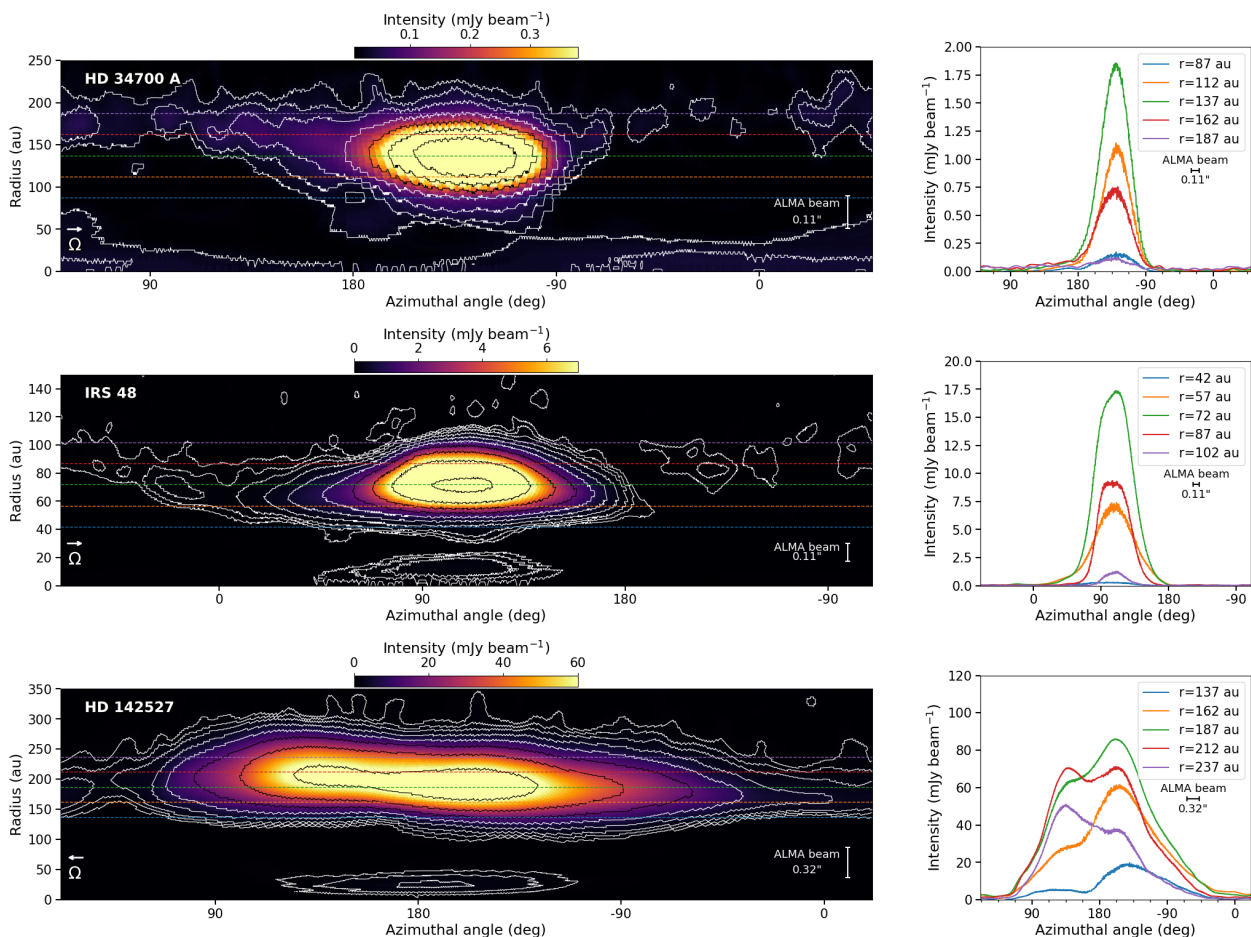


Fig. 2: Left column: de-projected continuum images of HD 34700 A (top), IRS 48 (middle) and HD 142527 (bottom) in polar coordinates. Contours are the same as in Figure 1. In the bottom left corner we show the rotation direction of the gas, while in the bottom right corner we show the beam size in the radial direction. Right column: Azimuthal profiles of the de-projected continuum images from the left column, taken at different radii around the peak location, corresponding to the dashed lines with the same colours in the left column. We use the `savgol_filter` function of the `scipy` (Virtanen et al. 2020) module to smooth the oscillations introduced by the interpolation on the polar grid. We also show the ALMA beam size associated to the azimuthal profile evaluated at the peak radius. The plots have been shifted azimuthally so that the image peak is in the centre and the -180° azimuth coincide with the 180° azimuth.

$$\Sigma(R, y) = \Sigma_g(R) \frac{1 + (A_{\text{gas}} - 1) \exp\left(-\frac{y^2}{2R^2\sigma_y^2}\right)}{1 + (A_{\text{gas}} - 1) \frac{\sigma_y}{2\sqrt{2\pi}} \text{Erf}\left(\frac{\sqrt{2\pi}}{\sigma_y}\right)}, \quad (5)$$

with $y = R\theta$ the azimuthal coordinate along the ring, A_{gas} the gas overdensity contrast, σ_y its azimuthal width, Erf the error function, and the normalisation is chosen so that the azimuthal average of the surface density would be its radial profile. In addition to the surface density parameters A_{gas} and σ_y , the analytical model of Birnstiel et al. (2013) depends also on the viscosity α , the maximum grain size a_{max} , the fragmentation velocity v_{frag} and the dust-to-gas volume ratio ϵ . Then, by visually comparing the observed Stokes number measured from their discs with the model prediction, van der Marel et al. (2021) found that the best set of parameters describing their sample, including IRS 48 and HD 142527, was: $A_{\text{gas}} = 1.2$, $\sigma_y = 10^\circ$, $\alpha = 10^{-3}$, $a_{\text{max}} = 1$ mm, $v_{\text{frag}} = 5$ ms $^{-1}$ and $\epsilon = 0.1$. However, they also specify the presence of degeneracies in the parameter space, for example between viscosity, dust-to-gas ratio and/or gas overdensity, or the

use of either a grain size distribution with a fixed maximum grain size or the steady-state equilibrium model from Birnstiel et al. (2011).

We follow the same approach to compute the emission azimuthal profile and reproduce our new HD 34700 A data, assuming a power law gas surface density radial profile $\Sigma_g(R) = \Sigma_c(R/R_c)^{-1}$ and evaluating Eq. 5 at the radial location of the peak intensity maximum R_{peak} . We assume the steady-state dust distribution from Birnstiel et al. (2011) for the dust population and we compute the optical depth $\tau = \sum_i \Sigma_i \kappa_{\text{abs},i}$, with Σ_i and $\kappa_{\text{abs},i}$ the surface density and “DSHARP”-mixture absorption opacity associated with grains of size i , taken from Birnstiel et al. (2018), and finally obtain the intensity profile of the emission $I_\nu = B_\nu(T_{\text{dust}})(1 - e^{-\tau})$, assuming a vertically isothermal disc with radial profile $T_{\text{dust}} = T_c(R/R_c)^{-0.5}$, with $T_c = 20$ K at $R_c = 100$ au.

In Figure 4, we show the observed azimuthal profile at the radial location of the peak intensity (137 au) and the intensity profile of the model, obtained by manually changing the input parameters until visually reproducing the observed profile. Although the parameter space is highly degenerate, as discussed in

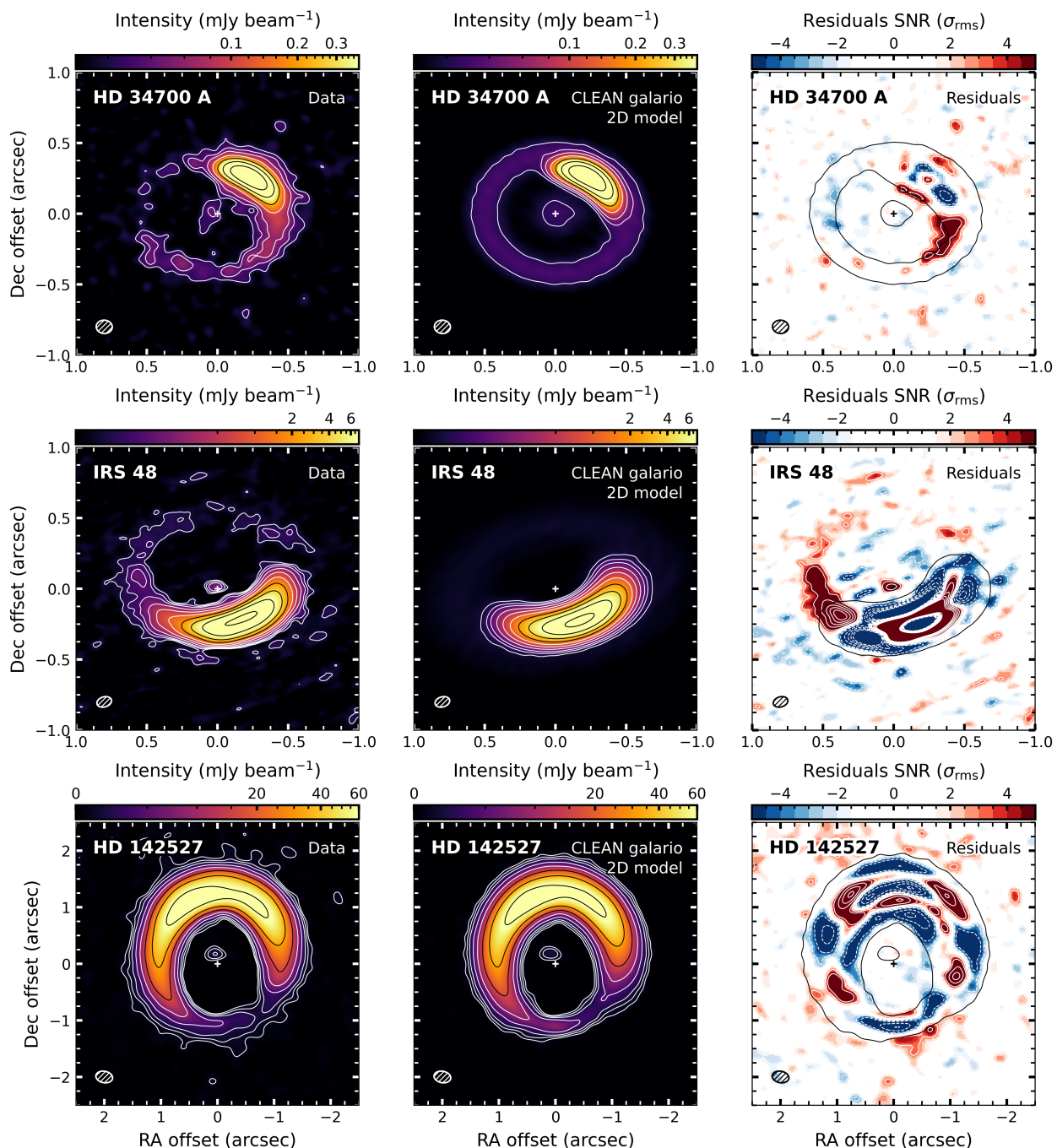


Fig. 3: Top to bottom: Images of HD 34700 A; IRS 48; HD 142527. Left to right: Continuum images, same as in Figure 1; CLEANed galarío model images; CLEANed residual images; In the left and middle columns, contours are the same as in Figure 1. In the right column, white solid (positive) and dashed (negative) contours start at 3σ and 5σ , and increase by 5σ , while black contours correspond to the 3σ emission from the CLEANed model.

van der Marel et al. (2021), we can constrain some of the parameters under the assumption that the dust overdensity is caused by a vortex. In fact, vortices need low viscosity to be long lived ($\alpha \lesssim 10^{-4} - 10^{-3}$; Zhu & Stone 2014; Bae et al. 2015; Rometsch et al. 2021) and concentrate dust such that the dust-to-gas ratio is locally increased. As a result, we find that the observed azimuthal profile is best reproduced for the following choice of parameters: $A_{\text{gas}} = 1.1$, $\sigma_y = 75^\circ$, $\alpha = 5 \times 10^{-4}$, $\Sigma_c = 50 \text{ g cm}^{-2}$ at $R_c = 1 \text{ au}$, $v_{\text{frag}} = 5 \text{ ms}^{-1}$ and $\epsilon = 0.1$.

While this set of parameters results in a model matching the observed intensity azimuthal profile on a qualitative level, it should not be taken as a unique solution. Increasing (decreasing) the α viscosity produces a lower (higher) peak-to-valley ratio of the profile, while raising (reducing) either ϵ or Σ_g shifts the azimuthal profile upwards (downwards). The width of the azimuthal profile is proportional azimuthal width σ_y of the gas bump, whereas increasing (decreasing) the overdensity contrast A_{gas} increments (decrements) the peak-to-valley ratio of the profile and produces a narrower (wider) profile. As a result, dif-

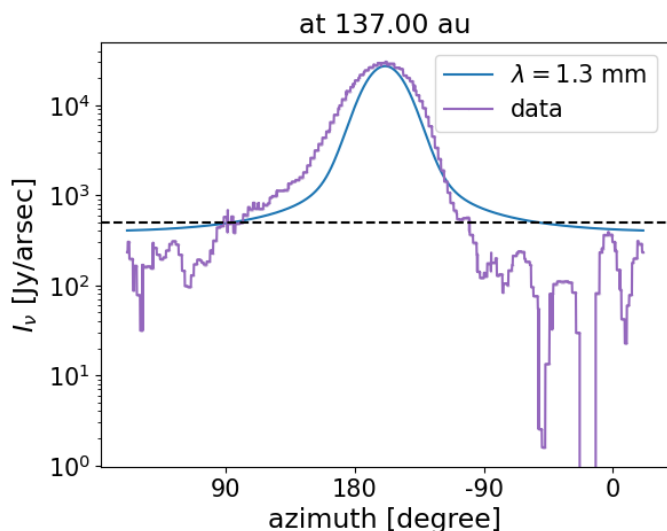


Fig. 4: Comparison between azimuthal profile of the observed dust emission at the radial location of the peak intensity (purple line) and model intensity azimuthal profile (blue line) for the HD 34700 A system. The black dashed line corresponds to the azimuthal average of the observed intensity at 170 au.

ferent combinations of the parameters might still reproduce the observed profile. However, with this analysis we do not aim to obtain a quantitative description of the observed profile, but to demonstrate that it is possible to reproduce it by invoking the dust trapping scenario.

Although this model can reproduce qualitatively the observed intensity azimuthal profile of the peak emission for the HD 34700 A system, it does not recover the elongated trailing tail that we see in Fig. 1 and 4. The asymmetric nature of the azimuthal profile might be indicative of dust segregation, with different sized dust grains trapped at different locations. This effect was shown in the simulations of Hammer et al. (2019), where they studied an elongated planet-induced vortex, featuring large grains concentrated close to the vortex centre and small grains circulating across the entirety of the vortex, producing an off-centred peak emission and a skewed azimuthal profile. Multi-wavelength observations are needed to confirm the dust segregation scenario and further assess the vortex origin of the asymmetric emission.

5.2. Origin of the asymmetry

A possible explanation for the high contrast continuum asymmetries observed in Figure 1 is gas anticyclonic vortices trapping dust in both the radial and azimuthal directions. Indeed, vortices have been suggested to be present in all the systems we consider in this work.

For IRS 48, van der Marel et al. (2013) reproduced the crescent by first simulating the gas distribution using FARGO3D, with a single sub-stellar companion carving the cavity for 1200 orbits, exciting RWI and producing a vortex. Then, starting from the resulting gas surface density, they computed the dust evolution and distribution with the model from Birnstiel et al. (2013), reproducing the observed contrast. Then, from polarimetric ALMA observations, Yang et al. (2024) inferred that the dust grains in the overdensity of IRS 48 are moderately settled, with a gas-to-dust scale height ratio of 2, and measured a turbu-

lent α parameter in the range $[10^{-4} - 5 \times 10^{-3}]$, consistent with the presence of a turbulent vortex. In HD 142527, Boehler et al. (2021) observed kinematic deviations from the gas Keplerian rotation in the ^{13}CO and C^{18}O line emission velocity maps, consistent with a ± 40 au, 200° large vortex, although a similar pattern might arise as a consequence of beam smearing in the presence of gas pressure gradients at the inner and outer edges of the disc. Multiple line, high resolution observations are needed to confirm either scenario. Finally, Stadler et al. (2026) recently analysed high resolution ($0''.1$) ALMA observations of ^{12}CO , ^{13}CO and C^{18}O lines in the system HD 34700 A. They find tentative evidence of an elongated Doppler flip co-located with the continuum asymmetry in ^{13}CO and C^{18}O , similarly to HD 142527 (Boehler et al. 2021), and model it as a kinematic signature of a vortex (Wölfer et al. 2025).

These three systems host very young (< 10 Myr) stars, which typically have a higher multiplicity fraction compared to main sequence stars (Offner et al. 2023). Both HD 34700 A and HD 142527 host a binary with a mass ratio $q > 0.05$, which naturally carve an eccentric cavity (Ragusa et al. 2017, 2020) with size of up to $(6a_{\text{bin}})$ (Penzlin et al. 2024, 2025; Sudarshan et al. 2022). However, with a binary separation of 0.69 au for HD 34700 A (Sterzik et al. 2005) and 10.8 au for HD 142527 (Nowak et al. 2024), the observed cavity sizes are too large to be explained by binary interaction alone, as shown by the simulations of HD 142527 in Penzlin et al. (2024).

Interestingly, a possible cause for the formation of a vortex is the presence of a planet carving the cavity (Bae et al. 2016; Lyra et al. 2009; de Val-Borro et al. 2007; Hammer & Lin 2023). Indeed, a massive companion would help the binaries of HD 34700 A and HD 142527, and the star in IRS 48 clear their large cavities, sustaining the RWI instability at its edge and triggering the formation of an anti-cyclonic vortex (Hammer et al. 2021). The presence of a planet might also explain the asymmetrical nature of the crescent we see in Figure 1 (Hammer et al. 2019). Notably, Hammer et al. (2017) have shown that slowly-growing planets trigger weaker but more elongated vortices, which, in combination with typical vortex lifetimes of $\lesssim 1000$ local orbits (Fung & Ono 2021; Rometsch et al. 2021), suggests that the object responsible for the observed vortex must not have migrated too far inwards from the current location of the vortex between its formation and today. Testing this scenario would require follow-up observations aiming to detect a companion within the disk cavity.

Infalling streamers hitting the disc are another mechanism that can produce vortices (Bae et al. 2015; Kuznetsova et al. 2022). While IRS 48 and HD 142527 show no evidence of interactions with the environment, Stadler et al. (2026) have suggested the presence of infalling streamers on the HD 34700 A disc from spectral line analysis of ^{12}CO . The strongest deviations from the disc rotation, probably associated to the location where the streamer hits the disc, are located in the vicinity of the dust crescent. It is unclear if the asymmetry in HD 34700 A is due to the infall, the presence of an undetected massive companion carving the cavity or a combination of the two.

HD 142527 is unique in that the asymmetry is best fit by two Gaussian curves in azimuth with our model. This configuration could be explained by either two recently-formed Rossby-wave-instability vortices that are in the process of coalescing, or the superposition of a vortex and the bright emission near the apocentre of an eccentric cavity (e.g., Penzlin et al. 2024; Calcino et al. 2019). The former scenario is highly unlikely due to its narrow time window. On the other hand, a massive companion could excite both an eccentric cavity (Kley & Dirksen 2006; Tanaka et al.

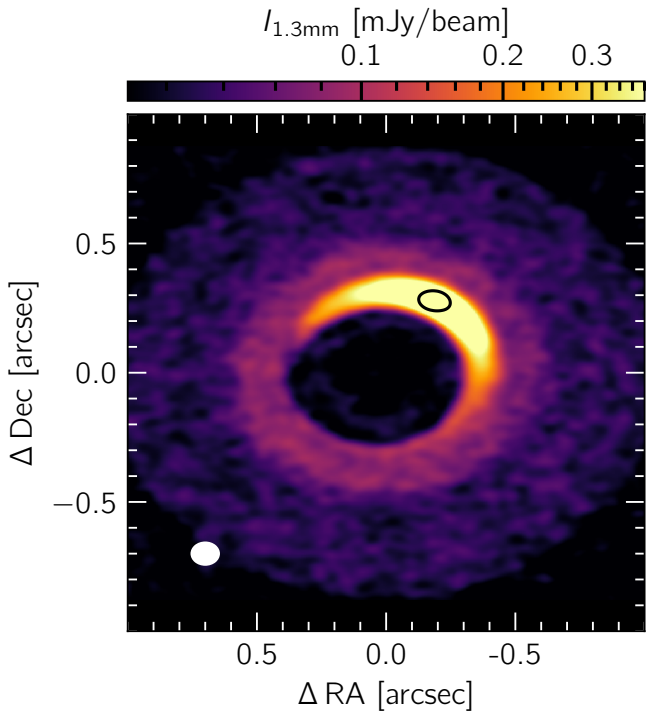


Fig. 5: Synthetic observation of an HD 34700 A analogue using a multi-fluid hydrodynamical simulation of a vortex. The emission is optically thin with the exception of the centre of the vortex (black circle after convolving). A slight tail is visible on the simulated vortex, similar to the observations of HD 34700 A and IRS 48.

2022) and a massive vortex on its edge, making it a favourable formation scenario in the absence of environmental factors such as infall.

5.3. Dust distribution around a massive vortex

In the previous paragraph we discussed several possible scenarios for the origin of the observed dust asymmetries, assuming they are vortices. Here, we would like to investigate the distribution of dust grains across the vortex, including the degree of asymmetry with respect to its centre, regardless of the origin of the vortex.

We model an HD 34700 A analogue using the hydrodynamics code PLUTO (Mignone et al. 2007) with a vertically-integrated, cylindrical ($\{R, \phi\}$) grid extending between $0.4\text{--}2.5 R_0$ in radius with $R_0 = 150$ au, and spanning the full 2π in azimuth, with $N_R \times N_\phi = 512 \times 1024$ cells and logarithmic spacing in radius. We utilize second-order spatial and temporal accuracy, the HLLC solver (Toro et al. 1994), a locally isothermal equation of state, the dust fluid module described in Ziampras et al. (2025), and the FARGO method to both improve numerical accuracy and drastically accelerate computations (Masset 2000; Mignone et al. 2012). The central object is modelled as a single star with $M_\star = 4 M_\odot$.

The numerical model is initialized with a disc of gas and dust that follow radial power-law profiles with $\Sigma_g = 1 \text{ g cm}^{-2} (R/R_0)^{-1}$ and $\Sigma_d = 0.01 \Sigma_g$, including a cavity interior to R_0 similar to Sudarshan et al. (2022), and an aspect ratio profile $h = 0.15 (R/R_0)^{1/4}$. Finally, we include viscous stress fol-

lowing Shakura & Sunyaev (1973) with $\alpha = 10^{-4}$ and a dust diffusion prescription following Weber et al. (2019).

We include six dust fluids with fixed grain sizes $a_d = \{10^{-4}, 0.001, 0.003, 0.01, 0.03, 0.1\}$ cm and bulk densities of $\bar{\rho} = 2.08 \text{ g cm}^{-3}$, coupled to the gas in the Epstein drag regime. The initial dust fluid densities are weighed such that $\Sigma_{d,i} \propto a_{d,i}^{q+4}$ with $q = -3.5$, corresponding to an MRN distribution (Mathis et al. 1977).

Our profile for h is quite in line with expectations beyond 100 au for typical disc parameters, even if possibly rather unrealistic for a passively irradiated disc with the particular stellar parameters for HD 34700 A. Nevertheless, given that we are aiming for a generic, proof-of-concept model, and that the cavity edge in HD 34700 A is anyway likely directly exposed to stellar irradiation (thus increasing the temperature and therefore h to values around 0.1–0.12), this choice is justified for our purposes.

With these initial conditions, the cavity edge at $\sim R_0$ is unstable to the Rossby-wave instability (Lovelace et al. 1999) and should collapse to a vortex. To form a massive vortex, we added a radially Gaussian distribution of gas and dust with a FWHM of $2H_0 = 0.3 R_0$ centred at R_0 , and seeded their velocity fields with noise of up to 1% of the local sound speed before integrating for 100 orbits at R_0 .

Immediately as the simulation begins, the cavity edge collapses into several vortices that coalesce into a single massive vortex over the first ~ 20 orbits. By the end of the simulation, a large, quasi-stable vortex has been established, with dust species of different sizes trapped at varying degree around it.

To produce the synthetic image at $\nu = 230$ GHz ($\lambda = 1.3$ mm) we compute the intensity at that frequency using

$$I_\nu(\mathbf{R}) = B(\nu, T) (1 - e^{-\tau_\nu}), \quad \tau_\nu(\mathbf{R}) = \sum_i \kappa_{\nu,i} \Sigma_{d,i}(\mathbf{R}), \quad (6)$$

which we then convolve with a beam of angular size $0''.114 \times 0''.094$ and layer with Gaussian noise convolved with the same beam and with an RMS of $7 \mu\text{Jy/beam}$. The result is shown in Fig. 5, using the same spatial extent and colorbar stretch as Fig. 1. We find that the synthetic image largely reproduces the features found around the cavity in the HD 34700 A system, with the emission around the vortex showing a (mild) asymmetrical tail (bottom right quadrant in the figure).

We note that the emission in our model can be rescaled to arbitrary radial scales and distances, provided that the dynamics of the gas and dust (related to h and the Stokes number $\text{St} \propto \bar{\rho} a_d / \Sigma_g$) are not changed. As a result, this model does not necessarily constrain the exact gas or dust properties around HD 34700 A beyond highlighting the requirement for large grains trapped in the vortex, which was already inferred in Sect. 5.1. Nevertheless, our model shows that non-axisymmetric emission with a large azimuthal extent can be easily (re)produced with a massive vortex, a structure that can naturally form in protoplanetary discs.

5.4. Disc eccentricity

Our *galario* models assume circular rings and arcs with no eccentricity. Yang et al. (2023) measured a high eccentricity of 0.27 in the dust ring of IRS 48, clearly motivated by the evident offset of the star with respect of the ring centre. In Figure 1 we mark the centre of the disc corrected with the *galario* offset, which is displaced with respect to the inner disc emission that surrounds

the central stars. This can be indicative of a non-zero eccentricity of the dust ring also in HD 34700 A and HD 142527, which is more evident in the polar maps in Figure 2. Indeed, the de-projected rings would appear as a straight horizontal line in these plots if they were circular, but instead the ring and the asymmetry peak at different radii, with the tail of the asymmetry connecting them spanning different radii. Additionally, azimuthal profiles taken at the same radial distance inward and outward from the peak intensity (see right column of Figure 2, comparing orange with red profiles and blue with purple profiles) are different from each other. This can be due to the possible eccentricity of the rings, or indicative of an asymmetric morphology of the rings and overdensities along the radial direction, or a combination of the two effects. Using numerical 3D hydrodynamical simulations, Price et al. (2018) showed that an eccentric circumbinary ring can be the result of an eccentric binary orbit. Later on, numerical studies from Ragusa et al. (2020); Penzlin et al. (2024) demonstrated that circumbinary disc can develop non zero eccentricity also in the case of a binary with a circular orbit, or as a consequence of the thermodynamical properties of the disc (Penzlin et al. 2025).

In order to measure the eccentricity of the discs, we expand Eqs.(1)-(3) to include eccentric rings and arcs. We parameterize the radial centre using:

$$r = a \frac{1 - e^2}{1 - e \cos(\phi - \omega)}, \quad (7)$$

where a is the semi-major axis of the ellipse, e its eccentricity and ω the argument of periastron. This parametrization assumes that the coordinate system is centred on the focus of the ellipse. We fix the eccentricity to be the same for all the ring and arc components in each disc model, and start the fitting procedure using these new parameters. We use the best-fit parameters we obtained for the circular models as initial guesses for the `galarío` runs with the eccentric models, using the same setup we introduced in Sec. 3.

The HD 34700 A model converges to a solution with $a = 529_{-3}^{+3}$ mas, $e = 0.109_{-0.004}^{+0.005}$, $\omega = 105_{-7}^{+7}$ deg, $\Delta RA = 99.6_{-0.3}^{+0.6}$ μ as, $\Delta Dec = 19_{-5}^{+6}$ μ as and the remaining parameters compatible within 3σ with those of the circular model. In particular, we find an inclination $i = 35.3_{-0.5}^{+0.6}$ deg and position angle $PA = 90.0_{-0.6}^{+0.5}$, in remarkable agreement with the geometrical parameters of the circular model. We note that in this case we use wide priors for the geometrical parameters since the beginning of the fitting procedure. In the cases of IRS 48 and HD 142527, the eccentric `galarío` models do not reach convergence. This is possibly caused by the presence of the asymmetry, which is radially wider compared to the ring and obscures the cavity edge morphology, making it compatible with a wide range of parameters. This degeneracy prevents the MCMC procedure from converging on a well-constrained parameter set. The IRS 48 and HD 142527 datasets are more affected than HD 34700 A as their asymmetries are azimuthally wider.

In Appendix C we show the model and residuals images of the eccentric model, and compare them with the circular case. The offset of the central component in the eccentric model is possibly caused by the presence of emission between the inner disc component and the asymmetry. It is interesting to note that the residuals in both the eccentric and circular models do not show any substantial difference. This suggests that there is a degeneracy between the circular and eccentric model, and it is currently unclear if the disc around HD 34700 A is circular or eccentric.

6. Conclusions

In this paper we present new high resolution (0''11) ALMA band 6 (1.3 mm) continuum observations of the system HD 34700 A. We compare its emission to two other systems featuring a similar morphology, IRS 48 and HD 142527, and perform visibility modelling of the new ALMA data, while also improving existing models for the other two systems, using the code `galarío`. Our results are summarised as follows:

- In the continuum data of HD 34700 A we observe a cavity and resolve an asymmetric ring with a de-projected radius of 0''53 (186 au) and a peak intensity contrast of 62, making HD 34700 A the transition disc with the second most prominent continuum asymmetry detected by ALMA to date. The dust overdensity is asymmetric, with a tail trailing with respect to the rotation of the gas, and peaks at 0''39 (137 au), with a PA of 227° and an azimuthal extent of more than 180°.
- Our `galarío` model for HD 34700 A is in remarkable agreement with the data, with residuals of up to 7.4σ localised only in the region of the asymmetric tail. Based on our model, we measure an azimuthal FWHM of 43.2° for the asymmetry. The central emission is offset compared to the disc centre corrected with the `galarío` offset, suggesting that the ring is eccentric. We improve the existing `galarío` model for HD 142527 (van der Marel et al. 2021), retrieving the double peaked structure of the ring. In this case we observe residuals of up to 20.1σ (6.2% of peak intensity) all across the ring, an improvement by a factor ~ 6 compared to the previous model, implying that the morphology is more complex than the Gaussian prescription in our model. For IRS 48, instead, we obtain a model similar to that of van der Marel et al. (2021), failing to recover the ring emission. We measure residuals of up to 96σ and -150σ , corresponding to 8.6% and 13.5% of the peak intensity, respectively.
- We compare the continuum emission of the three transition discs with the most asymmetric rings. All systems have a large dust cavity that cannot be explained by binary-disc interaction alone, an inner emission offset with respect to the disc centre, indicative of an eccentric ring, and a high contrast overdensity with an asymmetric tail trailing with respect to the disc's rotation. The high azimuthal contrast of the asymmetries rules out the orbit clustering of eccentric cavities scenario (Ataiee et al. 2013). A vortex has been proposed to explain the origin of the dust asymmetry, through kinematic analysis for HD 34700 A (Stadler et al. 2026) and HD 142527 (Boehler et al. 2021), and dust polarization measurements for IRS 48 (Yang et al. 2024).
- We measure the eccentricity of the ring around HD 34700 A, adapting our visibility models to fit eccentric rings and arcs, finding an eccentricity of 0.109. However, the model show a degeneracy with the circular solution, thus our estimates do not confirm that the system is eccentric.
- Under the vortex assumption, we reproduce the observed azimuthal profile of the emission using the analytical dust model of Birnstiel et al. (2013), by manually changing the input parameters. However, we stress that this solution might not be unique, as the parameter space is highly degenerate, and serves the purpose of providing a qualitative idea for the physical parameters associated with the possible dust trapping vortex.
- A hydrodynamic model of a massive vortex yields qualitatively similar features to those found in HD 34700 A and, to an extent, IRS 48, in that the emission around the vortex shows a mild asymmetry between the leading and trailing

sides. In combination with the above point, this suggests that the vortex scenario is indeed a plausible explanation for these features.

We have shown that the observed asymmetry can be consistent with the dust trapping scenario. However, it is currently unclear which physical mechanism is causing the observed azimuthal asymmetric rings in the discs of HD 34700 A, IRS 48 and HD 142527. While the presence of a vortex might explain the observed signatures, and it has been tentatively proposed for all the systems we consider, an alternative explanation might lie in the presence of a gas overdensity induced by eccentric cavities due to binary companions (Shi et al. 2012; Ragusa et al. 2017; Miranda et al. 2017). In order to differentiate between the two scenarios, higher spatial resolution ($\lesssim 0''.1$) observations are needed to detect the rotational kinematic pattern of a vortex. At the same time, multi-wavelength observations of the dust continuum emission would constrain the distribution of dust grains with different sizes, which are expected to show a shift in the spatial location of the peak emission in the presence of a vortex (Cazzoletti et al. 2018).

Acknowledgements. DF acknowledges Clement Baruteau, Aleksandra Kuznetsova, Anibal Sierra, and Daniel Price for the helpful scientific discussions. DF also acknowledges Milou Temmink and Haifeng Yang for sharing the calibrated data of HD 142527 and IRS 48. MB acknowledges Marco Tazzari for the development of Galarío. This project has received funding from the European Research Council (ERC) under the European Union’s Horizon 2020 research and innovation programme (PROTOPLANETS, grant agreement No. 101002188). S.F. is funded by the European Union (ERC, UNVEIL, 101076613) and acknowledges financial contribution from PRIN-MUR 2022YP5ACE. ER acknowledges support from the European Union (ERC Starting Grant DiscEvol, project number 101039651). Views and opinions expressed are, however, those of the author(s) only and do not necessarily reflect those of the European Union or the European Research Council. Neither the European Union nor the granting authority can be held responsible for them. This paper makes use of the following ALMA data: ADS/JAO.ALMA#2013.1.00305.S, ADS/JAO.ALMA#2019.1.01059.S, ADS/JAO.ALMA#2022.1.00760.S. ALMA is a partnership of ESO (representing its member states), NSF (USA) and NINS (Japan), together with NRC (Canada), NSTC and ASIAA (Taiwan), and KASI (Republic of Korea), in cooperation with the Republic of Chile. The Joint ALMA Observatory is operated by ESO, AUI/NRAO and NAOJ.

References

- Andrews, S. M. 2020, *ARA&A*, 58, 483
 Andrews, S. M., Huang, J., Pérez, L. M., et al. 2018, *ApJ*, 869, L41
 Ataiee, S., Pinilla, P., Zsom, A., et al. 2013, *A&A*, 553, L3
 Bae, J., Hartmann, L., & Zhu, Z. 2015, *ApJ*, 805, 15
 Bae, J., Isella, A., Zhu, Z., et al. 2023, in *Astronomical Society of the Pacific Conference Series*, Vol. 534, *Protostars and Planets VII*, ed. S. Inutsuka, Y. Aikawa, T. Muto, K. Tomida, & M. Tamura, 423
 Bae, J., Zhu, Z., & Hartmann, L. 2016, *ApJ*, 819, 134
 Barge, P. & Sommeria, J. 1995, *A&A*, 295, L1
 Baruteau, C. & Zhu, Z. 2016, *MNRAS*, 458, 3927
 Benac, P., Matrà, L., Wilner, D. J., et al. 2020, *ApJ*, 905, 120
 Biller, B., Lacour, S., Juhász, A., et al. 2012, *ApJ*, 753, L38
 Birnstiel, T., Dullemond, C. P., & Pinilla, P. 2013, *A&A*, 550, L8
 Birnstiel, T., Dullemond, C. P., Zhu, Z., et al. 2018, *ApJ*, 869, L45
 Birnstiel, T., Ormel, C. W., & Dullemond, C. P. 2011, *A&A*, 525, A11
 Boehler, Y., Ménard, F., Robert, C. M. T., et al. 2021, *A&A*, 650, A59
 Boehler, Y., Weaver, E., Isella, A., et al. 2017, *ApJ*, 840, 60
 Bohn, A. J., Benisty, M., Perraut, K., et al. 2022, *A&A*, 658, A183
 Brown, J. M., Herczeg, G. J., Pontoppidan, K. M., & van Dishoeck, E. F. 2012, *ApJ*, 744, 116
 Bruderer, S., van der Marel, N., van Dishoeck, E. F., & van Kempen, T. A. 2014, *A&A*, 562, A26
 Calcino, J., Price, D. J., Pinte, C., et al. 2019, *MNRAS*, 490, 2579
 CASA Team, Bean, B., Bhatnagar, S., et al. 2022, *PASP*, 134, 114501
 Casassus, S., van der Plas, G. M., Perez, S., et al. 2013, *Nature*, 493, 191
 Cazzoletti, P., van Dishoeck, E. F., Pinilla, P., et al. 2018, *A&A*, 619, A161
 Claudi, R., Maire, A. L., Mesa, D., et al. 2019, *A&A*, 622, A96
 Columba, G., Rigliaco, E., Gratton, R., et al. 2024, *A&A*, 681, A19
 de Val-Borro, M., Artymowicz, P., D’Angelo, G., & Peplinski, A. 2007, *A&A*, 471, 1043
 Dong, R., van der Marel, N., Hashimoto, J., et al. 2017, *ApJ*, 836, 201
 Espaillat, C., Muzerolle, J., Najita, J., et al. 2014, in *Protostars and Planets VI*, ed. H. Beuther, R. S. Klessen, C. P. Dullemond, & T. Henning, 497–520
 Fairlamb, J. R., Oudmaijer, R. D., Mendigutía, I., Ilee, J. D., & van den Ancker, M. E. 2015, *MNRAS*, 453, 976
 Flaherty, K., Hughes, A. M., Simon, J. B., et al. 2020, *ApJ*, 895, 109
 Foreman-Mackey, D., Hogg, D. W., Lang, D., & Goodman, J. 2013, *PASP*, 125, 306
 Francis, L. & van der Marel, N. 2020, *ApJ*, 892, 111
 Fukagawa, M., Hashimoto, J., Tamura, M., & Seeds/Hiciao/Ircs/Ao188. 2013, in *Astronomical Society of the Pacific Conference Series*, Vol. 476, *New Trends in Radio Astronomy in the ALMA Era: The 30th Anniversary of Nobeyama Radio Observatory*, ed. R. Kawabe, N. Kuno, & S. Yamamoto, 157
 Fung, J. & Ono, T. 2021, *ApJ*, 922, 13
 Gaia Collaboration, Vallenari, A., Brown, A. G. A., et al. 2023, *Astronomy & Astrophysics*, 674, A1
 Hammer, M., Kratter, K. M., & Lin, M.-K. 2017, *MNRAS*, 466, 3533
 Hammer, M. & Lin, M.-K. 2023, *MNRAS*, 525, 123
 Hammer, M., Lin, M.-K., Kratter, K. M., & Pinilla, P. 2021, *MNRAS*, 504, 3963
 Hammer, M., Pinilla, P., Kratter, K. M., & Lin, M.-K. 2019, *MNRAS*, 482, 3609
 Huang, P., Isella, A., Li, H., Li, S., & Ji, J. 2018, *ApJ*, 867, 3
 Izquierdo, A. F., Stadler, J., Galloway-Sprietsma, M., et al. 2025, *ApJ*, 984, L8
 Izquierdo, A. F., Testi, L., Facchini, S., Rosotti, G. P., & van Dishoeck, E. F. 2021, *A&A*, 650, A179
 Kley, W. & Dirksen, G. 2006, *A&A*, 447, 369
 Kuznetsova, A., Bae, J., Hartmann, L., & Mac Low, M.-M. 2022, *ApJ*, 928, 92
 Lacour, S., Biller, B., Cheetham, A., et al. 2016, *A&A*, 590, A90
 Li, H., Colgate, S. A., & Lovelace, R. V. E. 2000, in *AAS/High Energy Astrophysics Division*, Vol. 5, *AAS/High Energy Astrophysics Division #5*, 02.15
 Long, F., Pinilla, P., Herczeg, G. J., et al. 2018, *ApJ*, 869, 17
 Lovelace, R. V. E., Li, H., Colgate, S. A., & Nelson, A. F. 1999, *ApJ*, 513, 805
 Lovell, J. B., Hales, A. S., Kennedy, G. M., et al. 2026, *A&A*, 705, A200
 Lyra, W., Johansen, A., Klahr, H., & Piskunov, N. 2009, *A&A*, 493, 1125
 Lyra, W. & Lin, M.-K. 2013, *ApJ*, 775, 17
 Marino, S., Gupta, V., Weber, P., et al. 2026, *A&A*, 705, A202
 Marino, S., Perez, S., & Casassus, S. 2015, *ApJ*, 798, L44
 Masset, F. 2000, *Astronomy and Astrophysics Supplement Series*, 141, 165
 Mathis, J. S., Rumpl, W., & Nordsieck, K. H. 1977, *ApJ*, 217, 425
 Mignone, A., Bodo, G., Massaglia, S., et al. 2007, in *JENAM-2007, “Our Non-Stable Universe”*, 96–96
 Mignone, A., Zanni, C., Tzeferacos, P., et al. 2012, *ApJS*, 198, 7
 Miranda, R., Muñoz, D. J., & Lai, D. 2017, *MNRAS*, 466, 1170
 Monnier, J. D., Harries, T. J., Bae, J., et al. 2019, *ApJ*, 872, 122
 Nowak, M., Rowther, S., Lacour, S., et al. 2024, *A&A*, 683, A6
 Offner, S. S. R., Moe, M., Kratter, K. M., et al. 2023, in *Astronomical Society of the Pacific Conference Series*, Vol. 534, *Protostars and Planets VII*, ed. S. Inutsuka, Y. Aikawa, T. Muto, K. Tomida, & M. Tamura, 275
 Penzlin, A. B. T., Booth, R. A., Nelson, R. P., Schäfer, C. M., & Kley, W. 2024, *MNRAS*, 532, 3166
 Penzlin, A. B. T., Ziampras, A., Kurtovic, N. T., Barraza-Alfaro, M., & Pinilla, P. 2025, *MNRAS*
 Pinilla, P., Benisty, M., & Birnstiel, T. 2012, *A&A*, 545, A81
 Price, D. J., Cuello, N., Pinte, C., et al. 2018, *MNRAS*, 477, 1270
 Ragusa, E., Alexander, R., Calcino, J., Hirsh, K., & Price, D. J. 2020, *MNRAS*, 499, 3362
 Ragusa, E., Dipierro, G., Lodato, G., Laibe, G., & Price, D. J. 2017, *MNRAS*, 464, 1449
 Ragusa, E., Lynch, E., Laibe, G., Longarini, C., & Ceppi, S. 2024, *A&A*, 686, A264
 Regály, Z., Juhász, A., Sándor, Z., & Dullemond, C. P. 2012, *MNRAS*, 419, 1701
 Robert, C. M. T., Méheut, H., & Ménard, F. 2020, *A&A*, 641, A128
 Rometsch, T., Ziampras, A., Kley, W., & Béthune, W. 2021, *A&A*, 656, A130
 Rosotti, G. P. 2023, *New A Rev.*, 96, 101674
 Scheuck, M. B., van Boekel, R., Henning, T., et al. 2026, *arXiv e-prints*, arXiv:2602.03393
 Schworer, G., Lacour, S., Huéramo, N., et al. 2017, *ApJ*, 842, 77
 Shakura, N. I. & Sunyaev, R. A. 1973, *A&A*, 24, 337
 Shi, J.-M., Krolik, J. H., Lubow, S. H., & Hawley, J. F. 2012, *ApJ*, 749, 118
 Stadler, J., Benisty, M., Zagaria, F., et al. 2026, *A&A*, 707, A160
 Sterzik, M. F., Melo, C. H. F., Tokovinin, A. A., & van der Bliek, N. 2005, *A&A*, 434, 671
 Strom, K. M., Strom, S. E., Edwards, S., Cabrit, S., & Skrutskie, M. F. 1989, *AJ*, 97, 1451
 Sudarshan, P., Penzlin, A. B. T., Ziampras, A., Kley, W., & Nelson, R. P. 2022, *A&A*, 664, A157
 Surville, C. & Mayer, L. 2019, *ApJ*, 883, 176
 Surville, C., Mayer, L., & Lin, D. N. C. 2016, *ApJ*, 831, 82

- Tanaka, Y. A., Kanagawa, K. D., Tanaka, H., & Tanigawa, T. 2022, *ApJ*, 925, 95
- Tazzari, M., Beaujean, F., & Testi, L. 2018, *MNRAS*, 476, 4527
- Teague, R. 2019, *The Journal of Open Source Software*, 4, 1632
- Teague, R., Benisty, M., Facchini, S., et al. 2025, *ApJ*, 984, L6
- Temmink, M., Booth, A. S., van der Marel, N., & van Dishoeck, E. F. 2023, *A&A*, 675, A131
- Toro, E. F., Spruce, M., & Speares, W. 1994, *Shock Waves*, 4, 25
- Torres, G. 2004, *AJ*, 127, 1187
- Uyama, T., Currie, T., Christiaens, V., et al. 2020, in *American Astronomical Society Meeting Abstracts*, Vol. 236, American Astronomical Society Meeting Abstracts #236, 304.05
- van der Marel, N., Birnstiel, T., Garufi, A., et al. 2021, *AJ*, 161, 33
- van der Marel, N., Pinilla, P., Tobin, J., et al. 2015, *ApJ*, 810, L7
- van der Marel, N., van Dishoeck, E. F., Bruderer, S., et al. 2016a, *A&A*, 585, A58
- van der Marel, N., van Dishoeck, E. F., Bruderer, S., et al. 2013, *Science*, 340, 1199
- van der Marel, N., van Dishoeck, E. F., Bruderer, S., et al. 2016b, in *IAU Symposium*, Vol. 314, *Young Stars & Planets Near the Sun*, ed. J. H. Kastner, B. Stelzer, & S. A. Metchev, 139–142
- Virtanen, P., Gommers, R., Burovski, E., et al. 2020, *scipy/scipy: SciPy 1.6.0*
- Weber, P., Pérez, S., Benítez-Llambay, P., et al. 2019, *ApJ*, 884, 178
- Wölfer, L., Barraza-Alfaro, M., Teague, R., et al. 2025, *ApJ*, 984, L22
- Wölfer, L., Facchini, S., van der Marel, N., et al. 2023, *A&A*, 670, A154
- Yang, H., Fernández-López, M., Li, Z.-Y., et al. 2023, *ApJ*, 948, L2
- Yang, H., Fernández-López, M., Li, Z.-Y., et al. 2024, *ApJ*, 963, 134
- Zhu, Z. & Stone, J. M. 2014, *ApJ*, 795, 53
- Ziampras, A., Sudarshan, P., Dullemond, C. P., et al. 2025, *MNRAS*, 536, 3322

Appendix A: Observations

Table A.1: Summary of the data used in this work.

Label	Project ID	Observation Date	Baselines [m]	Frequency [GHz]	Resolution [arcsec]	Max. Scale [arcsec]	References
HD 34700 A	2022.1.00760.S	2022 Oct 09	33–214	344–355	0.72	8.57	Stadler et al. (2026)
	2022.1.00760.S	2023 May 05 - Jun 02	158–1417	346–355	0.12	2.30	Stadler et al. (2026)

In Table A.1 we report the observing log associated to the ALMA datasets presented for the first time in this paper.

Appendix B: Visibility Modelling

Table B.1: galarío best fit parameters

Dataset	$\log_{10} f_0$ [Jy sr ⁻¹]	x_0 [mas]	y_0 [mas]	$\sigma_{r,0}$ [mas]	$\log_{10} f_1$ [Jy sr ⁻¹]	r_1 [mas]	$\sigma_{r,1}$ [mas]	$\log_{10} f_1^a$ [Jy sr ⁻¹]	r_1^a [mas]
HD 34700 A	$8.10^{+0.03}_{-0.03}$	–	–	130^{+6}_{-6}	$8.15^{+0.01}_{-0.01}$	525^{+2}_{-2}	84^{+3}_{-3}	$10.148^{+0.002}_{-0.002}$	394^{+2}_{-2}
IRS 48	–	–	–	–	$8.052^{+0.007}_{-0.007}$	719^{+4}_{-4}	172^{+3}_{-3}	$11.04432^{+0.00008}_{-0.00008}$	$420.5^{+0.3}_{-0.3}$
HD 142527	$10.2^{+0.1}_{-0.1}$	94^{+3}_{-3}	-159^{+2}_{-3}	34^{+4}_{-5}	$10.950^{+0.004}_{-0.005}$	$1122.29^{+0.03}_{-0.03}$	$3.22^{+0.03}_{-0.03}$	$10.6383^{+0.0008}_{-0.0008}$	$1202.4^{+0.3}_{-0.3}$

Dataset	$\sigma_{r,1}^a$ [mas]	θ_1^a [deg]	$\sigma_{\theta,11}^a$ [deg]	$\sigma_{\theta,1r}^a$ [deg]	$\log_{10} f_2^a$ [Jy sr ⁻¹]	r_2^a [mas]	$\sigma_{r,2}^a$ [mas]	θ_2^a [deg]	$\sigma_{\theta,21}^a$ [deg]
HD 34700 A	$27.8^{+0.2}_{-0.2}$	$327.7^{+0.3}_{-0.3}$	$23.5^{+0.1}_{-0.1}$	$13.2^{+0.1}_{-0.1}$	–	–	–	–	–
IRS 48	$72.13^{+0.02}_{-0.02}$	$197.34^{+0.05}_{-0.04}$	$28.37^{+0.03}_{-0.03}$	$29.49^{+0.02}_{-0.02}$	–	–	–	–	–
HD 142527	$141.1^{+0.2}_{-0.2}$	$298.06^{+0.04}_{-0.04}$	$18.56^{+0.04}_{-0.04}$	$51.14^{+0.04}_{-0.04}$	$10.7017^{+0.0001}_{-0.0001}$	$1318.1^{+0.2}_{-0.2}$	$184.08^{+0.06}_{-0.06}$	$227.23^{+0.02}_{-0.02}$	$29.74^{+0.02}_{-0.02}$

Dataset	$\sigma_{\theta,2r}^a$ [deg]	i [deg]	PA [deg]	ΔRa [mas]	ΔDec [mas]
HD 34700 A	–	$35.1^{+0.1}_{-0.1}$	$92.9^{+0.3}_{-0.3}$	$-0.048^{+0.001}_{-0.001}$	$0.014^{+0.001}_{-0.001}$
IRS 48	–	$50.996^{+0.003}_{-0.005}$	$100.12^{+0.04}_{-0.04}$	$83.8^{+0.3}_{-0.3}$	$107.8^{+0.2}_{-0.2}$
HD 142527	$61.0^{+0.1}_{-0.1}$	$29.079^{+0.004}_{-0.004}$	$182.96^{+0.03}_{-0.03}$	$-38.1^{+0.2}_{-0.2}$	$-154.6^{+0.2}_{-0.2}$

In Table B.1 we summarise the best fit parameters resulting from our visibility modelling of HD 34700 A, IRS 48, HD 142527 observations. We have adopted the following priors:

HD 34700 A = $\{\log_{10} f_0 = [1.0, 10.0], r_0 = [0.0, 0.15] \text{ arcsec}, \log_{10} f_1 = [1.0, 10.0], r_1 = [0.0, 1.0] \text{ arcsec}, \sigma_{r,1} = [0.0, 0.2] \text{ arcsec}, \log_{10} f_1^a = [1.0, 11.0], r_1^a = [0.0, 1.0] \text{ arcsec}, \sigma_{r,1}^a = [0.0, 0.2] \text{ arcsec}, \theta_1^a = [0.0, 360.0] \text{ arcsec}, \sigma_{\theta,11}^a = [0.0, 180.0] \text{ arcsec}, \sigma_{\theta,r1}^a = [0.0, 180.0] \text{ arcsec}, i = [35.0, 37.0] \text{ deg}, PA = [92.5, 93.5] \text{ deg}, \Delta Ra = [-0.1, 0.1] \text{ arcsec}, \Delta Dec = [-0.1, 0.1] \text{ arcsec}\}$,

IRS 48 = $\{\log_{10} f_1 = [1.0, 11.0], r_1 = [0.4, 1.0] \text{ arcsec}, \sigma_{r,1} = [0.0, 0.2] \text{ arcsec}, \log_{10} f_1^a = [1.0, 12.0], r_1^a = [0.4, 0.6] \text{ arcsec}, \sigma_{r,1}^a = [0.0, 0.2] \text{ arcsec}, \theta_1^a = [0.0, 360.0] \text{ arcsec}, \sigma_{\theta,11}^a = [0.0, 180.0] \text{ arcsec}, \sigma_{\theta,r1}^a = [0.0, 180.0] \text{ arcsec}, i = [49.0, 51.0] \text{ deg}, PA = [99.0, 101.0] \text{ deg}, \Delta Ra = [0.0, 0.5] \text{ arcsec}, \Delta Dec = [0.0, 0.5] \text{ arcsec}\}$,

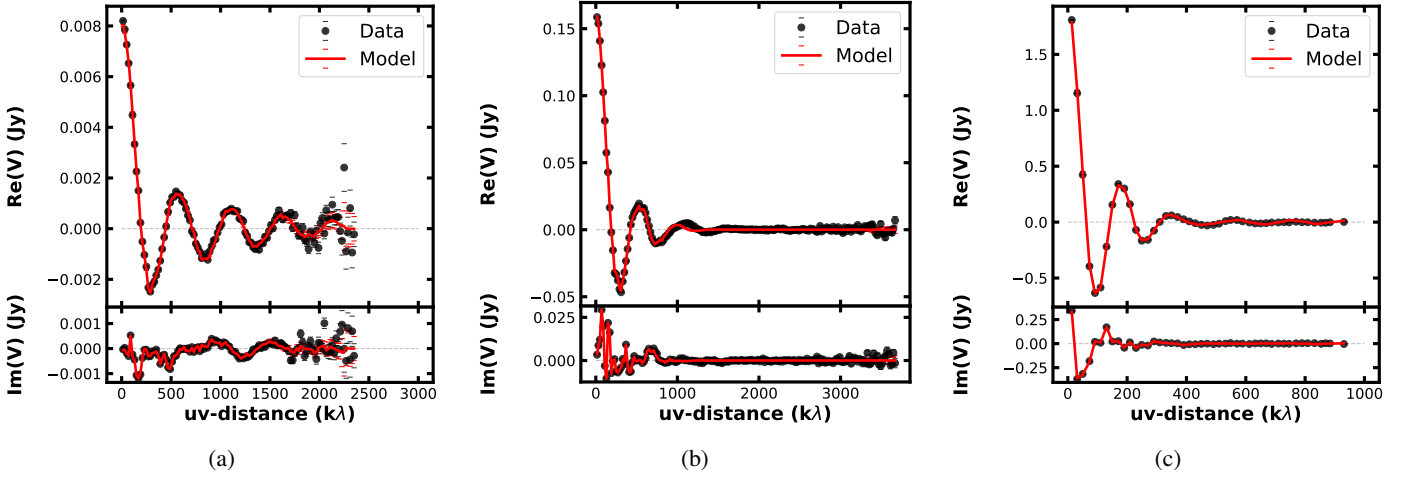


Fig. B.1: Real (top panel) and imaginary (bottom panel) parts of the re-centred and de-projected visibilities azimuthally averaged in bins with width of $20 k\lambda$ as a function of the de-projected baseline length for HD 34700 A (left), IRS 48 (middle) and HD 142527 (right). The black points represent the visibility data points, while the red solid line corresponds to the *galarío* best fit model.

$HD142527 = \{\log_{10} f_0 = [1.0, 12.0], x_0 = [-0.2, 0.2], y_0 = [-0.2, 0.2], r_0 = [0.0, 0.2] \text{ arcsec}, \log_{10} f_1^a = [1.0, 12.0], r_1^a = [0.0, 2.0] \text{ arcsec}, \sigma_{r,1} = [0.0, 0.8] \text{ arcsec}, \log_{10} f_1^a = [1.0, 12.0], r_1^a = [0.0, 2.0] \text{ arcsec}, \sigma_{r,1}^a = [0.0, 1.0] \text{ arcsec}, \theta_1^a = [0.0, 360.0] \text{ arcsec}, \sigma_{\theta,1}^a = [0.0, 180.0] \text{ arcsec}, \sigma_{\theta,r,1}^a = [0.0, 180.0] \text{ arcsec}, \log_{10} f_2^a = [1.0, 12.0], r_2^a = [0.0, 2.0] \text{ arcsec}, \sigma_{r,2}^a = [0.0, 1.0] \text{ arcsec}, \theta_2^a = [0.0, 360.0] \text{ arcsec}, \sigma_{\theta,2}^a = [0.0, 180.0] \text{ arcsec}, \sigma_{\theta,r,2}^a = [0.0, 180.0] \text{ arcsec}, i = [20.0, 40.0] \text{ deg}, PA = [150.0, 250.0] \text{ deg}, \Delta Ra = [-0.3, 0.3] \text{ arcsec}, \Delta Dec = [-0.3, 0.3] \text{ arcsec}\}.$

We choose narrow priors for the PA and inclination of HD 34700 A in order to be consistent with the analysis of Stadler et al. (2026), using the values resulting from their ^{13}CO discriminator fit as initial guesses to help achieve convergence. We follow the same approach for IRS 48, using the inclination and PA reported in Yang et al. (2023). At a later stage, we check that allowing for wider priors does not significantly change the geometrical parameters.

In Figure B.1 we show the azimuthally averaged visibility profiles for HD 34700 A, IRS 48 and HD 142527 (black dots) and the best fit *galarío* model (red solid line).

Appendix C: Eccentric model

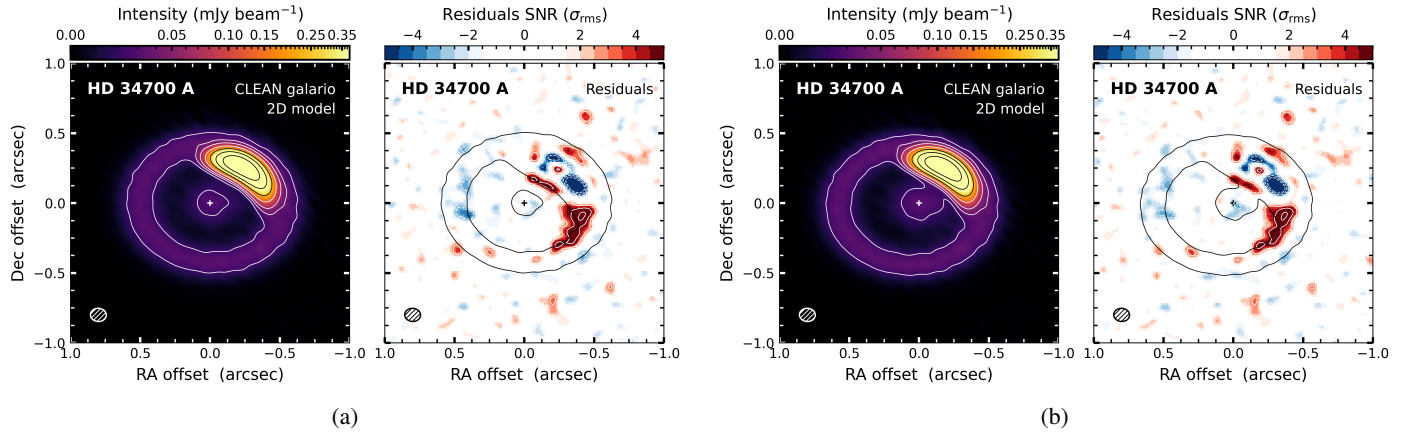


Fig. C.1: CLEANed images of the *galarío* model (left panel) and residuals (right panel) for the circular (a) and eccentric (b) models of HD 34700 A, same as middle and right columns of Fig. 3.

In Fig. C.1 we compare the *galarío* models and residuals of the HD 34700 A system, assuming a circular model (same as middle and right columns of Fig. 3), with those obtained assuming an eccentric model, as explained in Sec. 5.4.